Re-Analysis of Neutron Capture on ^{90,92}Zr at *s*-Process Energies

Zain Ul Abideen[1*], Abdul Kabir[1,2]

[1]*Department of Space Science, Institute of Space Technology, Islamabad 44000, Pakistan*

[2]*Space and Astrophysics Research Lab (SARL), National Center of GIS and Space Applications (NCGSA), Islamabad 44000, Pakistan*

A B S T R A C T

The Maxwellian-averaged cross sections (MACS) for the ^{90,92}Zr(n,γ)^{91,93}Zr processes were analyzed within the framework of the Hauser-Feshbach theory, making use of microscopic nuclear inputs. The effects of nuclear level densities and photon strength functions were studied for the mentioned isotopes. A comparison with the experimental data and KADoNiS was conducted at the s-process energies. Good agreement was achieved for both nuclear reactions under study. Finally, making use of the best-fit microscopic nuclear ingredients, we calculated the thermonuclear reaction rates, which show a reduction from the previously reported calculations.

Keywords: Nucleosynthesis, AGB stars, Massive stars, Statistical model, Nuclear level densities, Thermonuclear reaction rates

Introduction

The production of elements beyond the iron-peak occurs mainly through the neutron capture reactions. These are classified into *s*- and *r*-processes based on the neutron capture times [1]. The (slow) *s*-process is said to occur when the time for neutron capture is relatively greater than the time for beta decay. Under this constraint, the target nucleus for the neutron capture is ensured to be stable. This leads to the production of many isotopes being inaccessible through the *s*-process, and is in contrast to the (rapid) *r*-process, where the neutron capture times are lower than the beta decay times of the target nuclei. Nevertheless, the origin of about half of the elements heavier than iron, from *A*~56-204, can be attributed to the *s*-process [2]. There also exist approximately 30 stable, proton-rich nuclei known as the *p*-nuclei. These are hypothesized to be produced by the so-called *p*-process where their production is initiated by photodisintegration reactions on the products of neutron capture processes [3].

The energy production and the elemental synthesis in main-sequence stars are driven by the charged particle-induced reactions taking place inside their cores. This process can carry nucleosynthesis till iron (Fe) during later evolutionary stages, which has the highest binding energy per nucleon. After it, the Coulomb barrier becomes too large for these reactions to be sustained, and nucleosynthesis can only predominantly occur through neutrons. The *s*-process can occur in both low mass and massive stars. The main component of the *s*-process, responsible for the production of elements from A~90-204, occurs in low-mass AGB (asymptotic giant branch) stars, whereas the weak component responsible for the production of elements from the iron-peak nuclides to *A*~90, occurs in massive stars. The two components are distinguished based on the neutron sources they employ. In massive stars, the ^{22}Ne(α,n)^{25}Mg reaction produces a steady source of neutrons, and is hypothesized to occur during the helium-core burning and the carbon-shell burning phases [4]. In low-mass AGB stars, the temperature-dependent ^{22}Ne(α,n)^{25}Mg reaction rate is not high enough, and the neutron production is hypothesized to occur mainly through the ^{13}C(α,n)^{16}O process, which occurs in the intershell region. All AGB stars are expected to produce elements from mass numbers *A*~90-140, whereas only low-metallicity stars are hypothesized to create heavier elements (till *A*~204) [2].

This study focuses on the capture cross sections of the two zirconium (Zr) isotopes under investigation. Progress in theoretical modeling and experimental techniques has allowed researchers to probe nuclei and gain a better understanding of the production of heavier elements in stars. Both ^{90}Zr and ^{92}Zr are key to the production of heavier elements as they are associated with the first *s*-process peak in the abundance distribution around *A*=90. The isotopes share the magic and nearly magic number of neutrons (50, 52), and thus their cross sections add to the initial bottleneck from the iron-peak nuclides to beyond. The most recent experimental measurements for (n,γ) Maxwellian-averaged cross sections (MACS) were done by Tagliente *et al.* [5, 6]. The MACS were determined by folding the capture cross sections with the stellar spectra over a large neutron energy range. Their analyses lead to the reduction of the *s*-component of ^{92}Zr. Recently, Kabir *et al.* [4] analyzed the MACS of the ^{90,92}Zr(n,γ)^{91,93}Zr processes using phenomenological models for optical potential, nuclear level density, and radiative

---

strength (with the exception of the Gogny D1M model). They compared their finding with the available experimental data, and their adjusted results were in good agreement. They further calculated the thermonuclear reaction rates using the best-fit model combinations based upon the least calculated percentage error at the typical *s*-process temperature.

The phenomenological models rely on the introduction of free parameters, which can be adjusted to constrain the theoretical predictions. The primary goal of these models is to produce highly accurate results. In contrast, microscopic models prioritize a precise representation of underlying physics using minimal free parameters [7]. The phenomenological models are most suited for the applied domain of nuclear sciences, but microscopic models are preferable for nuclear astrophysics, where often high extrapolation capabilities are required. In the present study, we aim to investigate the predictions of microscopic nuclear inputs, including optical potential, level densities, and the radiative strengths, for the Maxwellian-averaged cross sections and the thermonuclear reaction rates. In the next sections, the framework and the discussions are presented, leading to the conclusion.

Theoretical Framework

Experimental data only cover a limited portion of the total nuclear data required for nucleosynthesis calculations. Nuclei with relevance to astrophysics generally have exotic origins and, thus, are difficult to study experimentally [8]. Only theoretical predictions, constrained by the available measurements, can be used to fill in the gaps. Neutron capture reactions beyond the iron-peak are studied within the framework of the Hauser-Feshbach theory, also known as the statistical model [9]. The capture cross sections are directly related to the transmission coefficients in the entrance and all exit channels. The transmission coefficients in the entrance channels are calculated using the optical model potential, which describes the interaction between the projectile and the target nucleus. For the case of capture reactions, the transmission coefficients for the emission of γ photons are given by the radiative strength functions. The nuclear level density needs to be folded in due to the large number of nuclear levels at excitation energies, when information about discrete levels is either missing or incomplete. The Hauser-Feshbach formula for binary cross section is given by

$$\sigma_{\alpha\alpha'}^{comp} = D^{comp} \frac{\pi}{k^2} \sum_{J=mod(I+s,1)}^{l_{max}+I+s} \sum_{\Pi=-1}^{1} \frac{(2J+1)}{(2I+1)(2s+1)}$$

$$\sum_{j=|(J-I)|}^{J+I} \sum_{l=|(J-s)|}^{j+s} \sum_{j'=|(J-I')|}^{J+I'} \sum_{l'=|(j'-s')|}^{j'+s'} \delta_\pi(\alpha)\delta_\pi(\alpha')$$

$$\frac{T_{\alpha l j}^J(E_a)\langle T_{\alpha'l'j'}^J(E_{a'})\rangle}{\sum_{\alpha'',l'',j''} \delta_\pi(\alpha'')\langle T_{\alpha''l''j''}^J(E_{a''})\rangle} W_{\alpha l j \alpha'l'j'}^J$$

where the following energy, angular momentum, and parity conservation laws need to be obeyed,

$$E_a + E_x + S_a = E_{a'} + E_{x'} + S_{a'} = E^{tot}$$
$$s + I + l = s' + I' + l' = J$$
$$\pi_o \Pi_o (-1)^l = \pi_f \Pi_f (-1)^{l'} = \Pi.$$

In the above equations, the symbols have the following meaning:

E_a is the energy of the projectile,

l is the orbital angular momentum of the projectile,

s is the spin of the projectile,

j is the total angular momentum of the projectile,

π_0 is the parity of the projectile,

$\delta_\pi(\alpha)$ is *1* if *$(-1)^l\pi_0\Pi_0 = \Pi$, 0* otherwise to enforce parity conservation,

α is the designation of the channel for the initial projectile-target system:

$\alpha = \{a, s, E_a, E_x, I, \Pi_0\}$, where *a* and E_x are the type of the projectile and the excitation energy (which is usually zero) of the target nucleus, respectively,

l_{max} is the maximum *l*-value of the projectile,

S_a is the separation energy,

$E_{a'}$ is the energy of the ejectile,

l' is the orbital angular momentum of the ejectile,

s' is the spin of the ejectile,

j' is the total angular momentum of the ejectile,

π_f is the parity of the ejectile,

$\delta_\pi(\alpha')$ is *1* if *$(-1)^{l'}\pi_f\Pi_f = \Pi$, 0* otherwise to enforce parity conservation,

α' is the designation of channel for the ejectile-residual nucleus final system:

$\alpha' = \{a', s', E_{a'}, E_x, I', \Pi_f\}$, where *a'* and E_x are the type of the ejectile and the residual nucleus excitation energy, respectively,

I is the spin of target nucleus,

Π_0 is the parity of target nucleus,

I' is the spin of residual nucleus,

Π_f is the parity of residual nucleus,

J is the total angular momentum of the compound system,

Π is the parity of the compound system,

D^{comp} is the depletion factor so as to take into account the pre-equilibrium and direct effects,

k is the wave number of the relative motion,

T is the transmission coefficient,

W is the correction factor for width fluctuation.

The preferred implementation of the Hauser-Feshbach theory was the TALYS 2.02 code [10]. It includes all reaction mechanisms involved in the study of light particle-induced nuclear reactions. The code's predictions have been tested on many nuclei of astrophysical interest by many authors [3, 4, 11, 12]. Phenomenological and microscopic options are available for all nuclear inputs (optical models, level densities, and radiative strengths). The microscopic option for the optical model includes the model of Jeukenne-Lejeune-Mahaux (JLM) [13]. For the level densities, the microscopic options include the Skyrme-Hartree-Fock-Bogoliubov model (SHFB), Gogny-Hartree-Fock-Bogoliubov model (GHFB), and the temperature-dependent Gogny-Hartree-Fock-Bogoliubov model (TGHFB). Finally, for the radiative strengths, the microscopic options include, but are not limited to, the Skyrme-Hartree-Fock-BCS model (HFBCS), the temperature-dependent relativistic mean-field model (TRMF), and the Gogny HFB+QRPA model with D1M interaction (D1M) [14].

The Maxwellian-averaged cross section (MACS) is used when the energies of projectiles follow a Maxwellian distribution, just as is the case with stellar environments. At the conditions in AGB and massive stars ($n_n \sim 10^9$ cm^{-3} and $kT \sim 30$ keV), both the Fermi-Dirac and the Bose-Einstein distributions reduce to the Maxwell-Boltzmann distribution [15]. Under these conditions, the high-energy tail of the Fermi-Dirac and Bose-Einstein distributions becomes negligible due to frequent particle interactions.

$$\langle\sigma\rangle(kT) = \frac{2}{\sqrt{\pi}(kT)^2} \int_0^\infty E\,\sigma(E)\,exp\left(\frac{-E}{kT}\right) dE,$$

where k is the Boltzmann constant, T is the temperature, $\sigma(E)$ is the capture cross section, and E is the projectile energy. The thermonuclear reaction rates per particle pair can be obtained from these MACS by multiplying with the mean velocity v_T at the temperature T [16].

Results and Discussions

To begin our analysis, we performed the computations for the MACS of ^{90}Zr(n,γ)^{91}Zr and ^{92}Zr(n,γ)^{93}Zr processes using the microscopic model combinations mentioned above.

The Zr isotopes employed in our study have the magic and nearly magic neutron numbers, which result in their low capture cross sections and consequently large abundances. For each nuclear reaction, the optical model was constrained, and the models for level densities and photon strengths were iterated. For low-energy neutrons as projectiles, the effects of changing the optical model can be ignored in favor of the other two components, the level densities and the photon strengths [11].

The level density model was first fixed for the 90Zr(n,γ)91Zr reaction, and the photon strengths (HFBCS, TRMF, D1M) were iterated. The results are shown in *Figure 1*. First, we calculated the deviation from the experimental data at the typical *s*-process energy of kT=30 keV. At this energy, the MACS using the SHFB level densities were 17.97 mb (HFBCS), 16.13 mb (TRMF), and 16.99 mb (D1M). The measurement of Tagliente *et al.* [5] at this energy was 19.30 mb. The percentage differences were 7.4%, 19.6%, and 13.6%, respectively. Similarly, at kT=30 keV, the MACS using the GHFB level densities were 16.05 mb (HFBCS), 14.37 mb (TRMF), and 23.02 mb (D1M). The percentage differences were 20.2%, 34.3%, and 19.3%, respectively. Finally, at kT=30 keV, the MACS using the TGHFB level densities were 11.26 mb (HFBCS), 10.27 mb (TRMF), and 12.90 mb (D1M). The percentage differences were 71.4%, 87.9%, and 49.6%, respectively. Among all cases, the photon strengths combined with the SHFB level densities produced the best results, while the TGHFB level densities produced the worst.

The same set of level densities and photon strengths were employed for the ^{92}Zr(n,γ)^{93}Zr reaction. The results have been shown in *Figure 2*. At kT=30 keV, the MACS using the SHFB level densities were 34.31 mb (HFBCS), 29.31 mb (TRMF), and 27.71 mb (D1M). The measurement of Tagliente *et al.* [6] at this energy was 38.10 mb. The percentage differences were 11.0%, 29.9%, and 37.5%, respectively. Similarly, at kT=30 keV, the MACS using the GHFB level densities were 28.47 mb (HFBCS), 24.48 mb (TRMF), and 34.59 mb (D1M). The percentage differences were 33.8%, 55.6%, and 10.1%, respectively. Finally, at kT=30 keV, the MACS using the TGHFB level densities were 36.49 mb (HFBCS), 31.49 mb (TRMF), and 32.35 mb (D1M). The percentage differences were 4.4%, 20.9% and 17.8%, respectively. Among all cases, the photon strengths combined with the TGHFB level densities produced the best results, followed by the SHFB

predictions. It is also noted that the agreement with the experimental data deviates by a factor of 1.5 at higher energies.
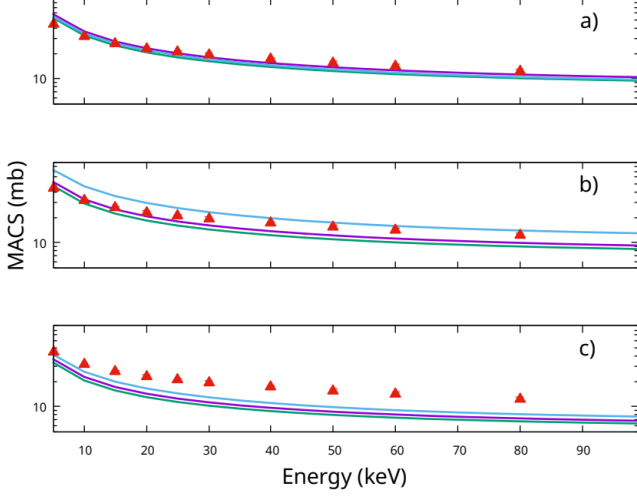

Fig. 1   The calculated MACS using the a) SHFB b) GHFB c) TGHFB level densities for the ^{90}Zr(n,γ)^{91}Zr process along with the comparison data. The solid lines colored purple, green, and cyan represent the HFBCS, TRMF, and D1M models of photon strengths, respectively. The red triangles represent the experimental data of Tagliente *et al.* [5].
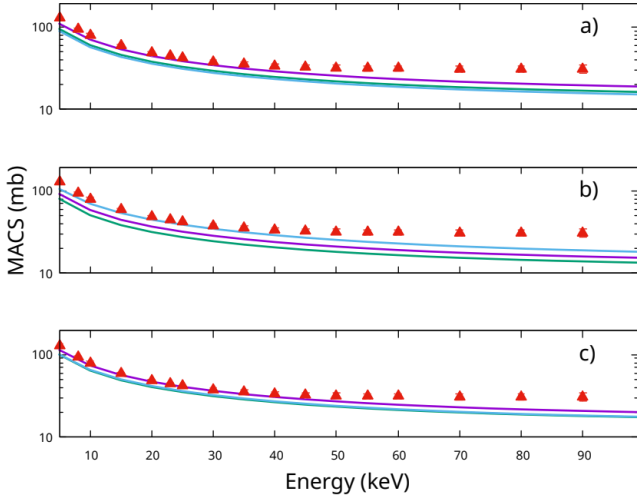

Fig. 2   The calculated MACS using the a) SHFB b) GHFB c) TGHFB level densities for the ^{92}Zr(n,γ)^{93}Zr process along with the comparison data. The solid lines colored purple, green, and cyan represent the HFBCS, TRMF, and D1M models of photon strengths, respectively. The red triangles represent the experimental data of Tagliente *et al.* [6].

Table 1. The comparison of calculated MACS for the ^{90}Zr(n,γ)^{91}Zr process with those from KADoNiS at the typical *s*-process energy *kT*=30 keV.

Level Density	Photon Strength	MACS	KADoNiS	Δ
SHFB	HFBCS	17.97	19.3	7.4%
SHFB	TRMF	16.13	19.3	19.7%
SHFB	D1M	16.99	19.3	13.6%
GHFB	HFBCS	16.05	19.3	20.2%
GHFB	TRMF	14.37	19.3	34.3%
GHFB	D1M	23.02	19.3	19.3%
TGHFB	HFBCS	11.26	19.3	71.4%
TGHFB	TRMF	10.27	19.3	87.9%
TGHFB	D1M	12.90	19.3	49.6%

Table 2. The comparison of calculated MACS for the ^{92}Zr(n,γ)^{93}Zr process with those from KADoNiS at the typical *s*-process energy *kT*=30 keV.

Level Density	Photon Strength	MACS	KADoNiS	Δ
SHFB	HFBCS	34.31	30.1	13.9%
SHFB	TRMF	29.31	30.1	2.7%
SHFB	D1M	27.71	30.1	8.6%
GHFB	HFBCS	28.47	30.1	5.7%
GHFB	TRMF	24.48	30.1	22.9%
GHFB	D1M	34.59	30.1	14.9%
TGHFB	HFBCS	36.49	30.1	21.6%
TGHFB	TRMF	31.49	30.1	4.6%
TGHFB	D1M	32.35	30.1	7.5%

Additionally, we have performed a comparison of our microscopic calculations of MACS with those of Karlsruhe Astrophysical Database of Nucleosynthesis in Stars (KADoNiS) [17]. The analysis based on percentage deviation for ^{90}Zr(n,γ)^{91}Zr process has been presented in *Table 1*, while that for the ^{92}Zr(n,γ)^{93}Zr process is in *Table 2*. The results of this comparison are in agreement with the analysis performed with the experimental measurement. For the ^{90}Zr(n,γ)^{91}Zr process, the SHFB level densities produced the best results, while the TGHFB level densities performed the worst. For the ^{92}Zr(n,γ)^{93}Zr process, SHFB level densities again produced the best results, followed closely by TGHFB level densities. Interestingly, for this case, all model combinations produced results with percentage differences less than 25%.

Lastly, using the best-fit microscopic model combinations, we have computed the thermonuclear reaction rates up to a temperature of T_9=0.5 as depicted in *Figure 3*. Collections of reaction rates, commonly referred to as libraries, are core nuclear physics inputs to the theoretical studies of the nucleosynthesis environments [18]. The effects of magic neutron numbers on the rates are clearly illustrated. The rates of the ^{92}Zr(n,γ)^{93}Zr process are higher because the nearly magic neutron numbers offer little resistance to the incoming neutrons in contrast to the ^{90}Zr(n,γ)^{91}Zr process. The microscopic descriptions suggest a lower reaction rate for ^{92}Zr(n,γ)^{93}Zr at $T_9 < 0.2$, while for the ^{90}Zr(n,γ)^{91}Zr process, the rates are found to be systematically lower at all temperatures.

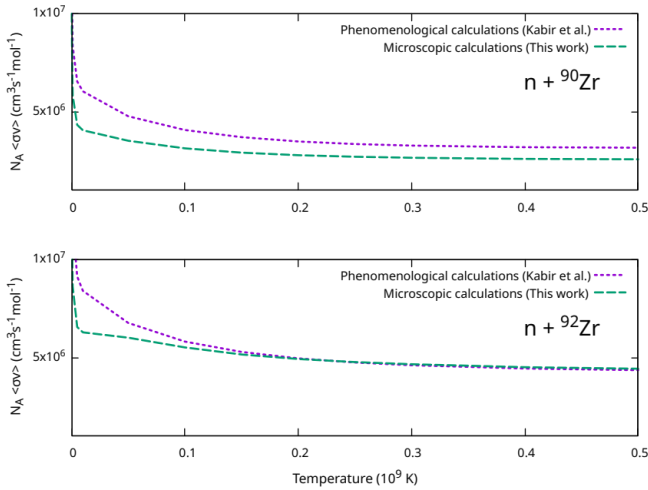Fig. 3   The thermonuclear reaction rates for the ^{90,92}Zr(n,γ)^{91,93}Zr processes using the best fit microscopic and phenomenological model combinations, up to a temperature of T$_9$=0.5.

Conclusion

In conclusion, we have studied the neutron capture reactions on the isotopes of Zr with mass numbers *A*=90 and *A*=92 using microscopic models for the optical potential, nuclear level density, and photon strength. Our analyses included comparisons with the available experimental data and with KADoNiS. The results obtained using the microscopic nuclear inputs were within the acceptable range, which makes them preferable over the results of adjusted phenomenological models. For ^{90}Zr, the photon strengths combined with the SHFB level densities provided the best agreement. In contrast, for ^{92}Zr, model combinations gave a systematic deviation at higher energies while agreeing at the standard *s*-process energy of *kT*=30 keV. The best-fit reaction rates were found to be lower than the phenomenological ones for both nuclear reactions, suggesting a slower *s*-process flow. The constrained microscopic reaction rates reported in our study can be incorporated in elemental abundance models for improved predictions.

References

[1] E. M. Burbidge, G. R. Burbidge, W. A. Fowler, and F. Hoyle, "Synthesis of the elements in stars," *Rev. Mod. Phys.*, vol. 29, no. 4, pp. 547, 1957.

[2] S. Goriely and L. Siess, "The s-process Nucleosynthesis," *Proc. Int. Astron. Union*, vol. 1, no. S228, pp. 451–460, 2005.

[3] M. Eroğlu, C. Yalçın, and R. T. Güray, "Investigation of the 121Sb (α, γ) 125I reaction cross-section calculations at astrophysical energies," *Nucl. Sci. Tech.*, vol. 34, no. 11, pp. 168, 2023.

[4] A. Kabir, Z. U. Abideen, J.-U. Nabi, and D. Khan, "Investigation of 90, 92Zr (n, γ) 91, 93Zr in the s-process nucleosynthesis," *Z. Naturforsch. A*, vol. 79, no. 5, pp. 489–496, 2024.

[5] G. Tagliente *et al.*, "Neutron capture cross section of Zr 90: Bottleneck in the s-process reaction flow," *Phys. Rev. C*, vol. 77, no. 3, pp. 035802, 2008.

[6] G. Tagliente *et al.*, "The Zr 92 (n, γ) reaction and its implications for stellar nucleosynthesis," *Phys. Rev. C*, vol. 81, no. 5, pp. 055801, 2010.

[7] N. N. Le, S. Cristallo, D. Vescovi, L. T. Phuc, and N. Q. Hung, "Maxwellian-averaged cross section of 181Ta (n, γ) reaction and its astrophysical implications," *Nucl. Phys. A*, vol. 1023, pp. 122450, 2022.

[8] S. Goriely, S. Hilaire, and A. J. Koning, "Improved predictions of nuclear reaction rates with the TALYS reaction code for astrophysical applications," *Astron. Astrophys.*, vol. 487, no. 2, pp. 767–774, 2008.

[9] W. Hauser and H. Feshbach, "The inelastic scattering of neutrons," *Phys. Rev.*, vol. 87, no. 2, pp. 366, 1952.

[10] A. J. Koning, S. Hilaire, and M. C. Duijvestijn, "TALYS: Comprehensive nuclear reaction modeling," in *AIP Conf. Proc.*, vol. 769, no. 1, pp. 1154–1159, 2005.

[11] A. Kabir, Z. U. Abideen, and J.-U. Nabi, "Re-investigation of Neutron Capture by 84 Kr and 86 Kr in the s-Process Nucleosynthesis," *Braz. J. Phys.*, vol. 54, no. 3, pp. 80, 2024.

[12] A. Kabir, M. Tahir, J. Nabi, Z. U. Abideen, and I. Mudassir, "Examination of Radiative capture Rates of 99Tc (n, γ) 100Tc and Stellar β-Decay Rates of 99Tc," *Res. Astron. Astrophys.*, 2025.

[13] E. Bauge, J. P. Delaroche, and M. Girod, "Semimicroscopic nucleon-nucleus spherical optical model for nuclei with A>~ 40 at energies up to 200 MeV," *Phys. Rev. C*, vol. 58, no. 2, pp. 1118, 1998.

[14] A. Koning, S. Hilaire, and S. Goriely, "TALYS: modeling of nuclear reactions," *Eur. Phys. J. A*, vol. 59, no. 6, pp. 131, 2023.

[15] H. Beer, F. Voss, and R. R. Winters, "On the calculation of Maxwellian-averaged capture cross sections," *Astrophys. J. Suppl. Ser.*, vol. 80, no. 1, pp. 403–424, 1992.

[16] A. Kabir, J.-U. Nabi, M. Tahir, A. Muneem, and Z. U. Abideen, "Re-analysis of temperature dependent neutron capture rates and stellar β-decay rates of 95-98Mo," *Chin. Phys. C*, vol. 48, no. 9, pp. 094101, 2024.

[17] I. Dillmann *et al.*, "The new KADoNiS v1.0 and its influence on the weak s-process nucleosynthesis," in *PoS (NIC XIII Conf.)*, vol. 57, 2014.

[18] M. S. Smith, "Nuclear data resources and initiatives for nuclear astrophysics," *Front. Astron. Space Sci.*, vol. 10, pp. 1243615, 2023.